

OPEN ACCESS

Repository of the Max Delbrück Center for Molecular Medicine (MDC) in the Helmholtz Association

<https://edoc.mdc-berlin.de/16764>

CuBe: parametric modeling of 3D foveal shape using cubic Bézier

Yadav, S.K., Motamedi, S., Oberwahrenbrock, T., Oertel, F.C., Polthier, K., Paul, F., Kadas, E.M., Brandt, A.U.

NOTICE: this is a copy of the original article as published under the Copyright Transfer and Open Access Publishing Agreement (OAPA) of the Optical Society (OSA). The original article was first published in:

Biomedical Optics Express
2017 SEP 01 ; 8(9): 4181-4199
2017 AUG 22 (first published online)
doi: [10.1364/BOE.8.004181](https://doi.org/10.1364/BOE.8.004181)

Publisher: [The Optical Society \(OSA\)](https://www.optical-society.org/)

Copyright © 2017, Optical Society of America. Users may use, reuse, and build upon the article, or use the article for text or data mining, so long as such uses are for non-commercial purposes and appropriate attribution is maintained. All other rights are reserved.



CuBe: parametric modeling of 3D foveal shape using cubic Bézier

SUNIL KUMAR YADAV,^{1,2} SEYEDAMIRHOSEIN MOTAMEDI,¹ TIMM OBERWAHRENBROCK,¹ FREDERIKE COSIMA OERTEL,¹ KONRAD POLTHIER,² FRIEDEMANN PAUL,^{1,3,4} ELLA MARIA KADAS,^{1,*} AND ALEXANDER U. BRANDT¹

¹NeuroCure Clinical Research Center, Charité - Universitätsmedizin Berlin, Germany

²Mathematical Geometry Processing Group, Freie Universität Berlin, Germany

³Department of Neurology, Charité - Universitätsmedizin Berlin, Germany

⁴Experimental and Clinical Research Center, Max Delbrück Center for Molecular Medicine and Charité - Universitätsmedizin Berlin, Germany

*ella-maria.kadas@charite.de

Abstract: Optical coherence tomography (OCT) allows three-dimensional (3D) imaging of the retina, and is commonly used for assessing pathological changes of fovea and macula in many diseases. Many neuroinflammatory conditions are known to cause modifications to the fovea shape. In this paper, we propose a method for parametric modeling of the foveal shape. Our method exploits invariant features of the macula from OCT data and applies a cubic Bézier polynomial along with a least square optimization to produce a best fit parametric model of the fovea. Additionally, we provide several parameters of the foveal shape based on the proposed 3D parametric modeling. Our quantitative and visual results show that the proposed model is not only able to reconstruct important features from the foveal shape, but also produces less error compared to the state-of-the-art methods. Finally, we apply the model in a comparison of healthy control eyes and eyes from patients with neuroinflammatory central nervous system disorders and optic neuritis, and show that several derived model parameters show significant differences between the two groups.

© 2017 Optical Society of America

OCIS codes: (100.0100) Image processing; (100.2960) Image analysis; (110.4500) Optical coherence tomography; (000.4430) Numerical approximation and analysis.

References and links

1. D. Huang, E. Swanson, C. Lin, J. Schuman, W. Stinson, W. Chang, M. Hee, T. Flotte, K. Gregory, C. Puliafito, and a. et, "Optical coherence tomography," *Science* **254**, 1178–1181 (1991).
2. N. M. Roth, S. Saidha, H. Zimmermann, A. U. Brandt, J. Isensee, A. Benkhellouf-Rutkowska, M. Dornauer, A. A. Kühn, T. Müller, P. A. Calabresi, and F. Paul, "Photoreceptor layer thinning in idiopathic parkinson's disease," *Movement Disorders* **29**, 1163–1170 (2014).
3. S. Stricker, T. Oberwahrenbrock, H. Zimmermann, J. Schroeter, M. Endres, A. U. Brandt, and F. Paul, "Temporal retinal nerve fiber loss in patients with spinocerebellar ataxia type 1," *PLoS ONE* **6**, e23024 (2011).
4. T. Oberwahrenbrock, M. Ringelstein, S. Jentschke, K. Deuschle, K. Klumbies, J. Bellmann-Strobl, J. Harmel, K. Ruprecht, S. Schippling, H.-P. Hartung, O. Aktas, A. U. Brandt, and F. Paul, "Retinal ganglion cell and inner plexiform layer thinning in clinically isolated syndrome," *Multiple Sclerosis Journal* **19**, 1887–1895 (2013).
5. L. J. Balk, P. Tewarie, J. Killestein, C. H. Polman, B. Uitdehaag, and A. Petzold, "Disease course heterogeneity and ocr in multiple sclerosis," *Multiple sclerosis (Houndmills, Basingstoke, England)* **20**, 1198–1206 (2014).
6. F. Pache, H. Zimmermann, J. Mikolajczak, S. Schumacher, A. Lacheta, F. C. Oertel, J. Bellmann-Strobl, S. Jarius, B. Wildemann, M. Reindl, A. Waldman, K. Soelberg, N. Asgari, M. Ringelstein, O. Aktas, N. Gross, M. Buttman, T. Ach, K. Ruprecht, F. Paul, A. U. Brandt, and in cooperation with the Neuromyelitis Optica Study Group (NEMOS), "Mog-igg in nmo and related disorders: a multicenter study of 50 patients. part 4: Afferent visual system damage after optic neuritis in mog-igg-seropositive versus aqp4-igg-seropositive patients." *J. Neuroinflammation* **13**, 282 (2016).
7. E. Schneider, H. Zimmermann, T. Oberwahrenbrock, F. Kaufhold, E. M. Kadas, A. Petzold, F. Bilger, N. Borisow, S. Jarius, B. Wildemann, K. Ruprecht, A. U. Brandt, and F. Paul, "Optical coherence tomography reveals distinct patterns of retinal damage in neuromyelitis optica and multiple sclerosis," *PLOS ONE* **8**, 1–10 (2013).
8. F. C. Oertel, J. Kuchling, H. Zimmermann, C. Chien, F. Schmidt, B. Knier, J. Bellmann-Strobl, T. Korn, M. Scheel, A. Klistorner, K. Ruprecht, F. Paul, and A. U. Brandt, "Microstructural visual system changes in

- AQP4-antibody-seropositive NMO, *Neurology - Neuroimmunology Neuroinflammation* **4**, e334 (2017).
9. T. Oberwahrenbrock, M. Weinhold, J. Mikolajczak, H. Zimmermann, F. Paul, I. Beckers, and A. U. Brandt, "Reliability of intra-retinal layer thickness estimates," *PLoS one* **10**, e0137316 (2015).
 10. R. Kafieh, H. Rabbani, and S. Kermani, "A review of algorithms for segmentation of optical coherence tomography from retina." *J. Medical Signals and Sensors* **3**, 45–60 (2013).
 11. S. Niu, Q. Chen, L. de Sisternes, D. L. Rubin, W. Zhang, and Q. Liu, "Automated retinal layers segmentation in sd-oct images using dual-gradient and spatial correlation smoothness constraint," *Computers in Biology and Medicine* **54**, 116–128 (2014).
 12. Y. M. Cha and J. H. Han, "High-accuracy retinal layer segmentation for optical coherence tomography using tracking kernels based on gaussian mixture model," *IEEE J. Sel. Top. Quantum Electron.* **20**, 32–41 (2014).
 13. L. Fang, D. Cunefare, C. Wang, R. H. Guymer, S. Li, and S. Farsiu, "Automatic segmentation of nine retinal layer boundaries in oct images of non-exudative amd patients using deep learning and graph search," *Biomed. Opt. Express* **8**, 2732–2744 (2017).
 14. S. Tick, F. Rossant, I. Ghorbel, A. Gaudric, J.-A. Sahel, P. Chaumet-Riffaud, and M. Paques, "Foveal shape and structure in a normal population," *Investigative Ophthalmology and Visual Science* **52**, 5105 (2011).
 15. T. Y. P. Chui, Z. Zhong, H. Song, and S. A. Burns, "Foveal avascular zone and its relationship to foveal pit shape," *Optometry and Vision Science* **89**, 602–610 (2012).
 16. D. X. Hammer, N. V. Iftimia, R. D. Ferguson, C. E. Bigelow, T. E. Ustun, A. M. Barnaby, and A. B. Fulton, "Foveal fine structure in retinopathy of prematurity: An adaptive optics fourier domain optical coherence tomography study," *Investigative Ophthalmology and Visual Science* **49**, 2061 (2008).
 17. B. K. McCafferty, M. A. Wilk, J. T. McAllister, K. E. Stepien, A. M. Dubis, M. H. Brilliant, J. L. Anderson, J. Carroll, and C. G. Summers, "Clinical insights into foveal morphology in albinism," *J. Pediatric Ophthalmology Strabismus* **52**, 167–172 (2015).
 18. Y. Barak, M. P. Sherman, and S. Schaal, "Mathematical Analysis of Specific Anatomic Foveal Configurations Predisposing to the Formation of Macular Holes," *Investigative Ophthalmology Visual Science* **52**, 8266–8270 (2011).
 19. B. Nesmith, A. Gupta, T. Strange, Y. Schaal, and S. Schaal, "Mathematical Analysis of the Normal Anatomy of the Aging Fovea Anatomy of the Aging Fovea," *Investigative Ophthalmology & Visual Science* **55**, 5962–5966 (2014).
 20. A. M. Dubis, J. T. McAllister, and J. Carroll, "Reconstructing foveal pit morphology from optical coherence tomography imaging," *Br. J. Ophthalmol.* **93**, 1223–1227 (2009).
 21. P. Scheibe, M. T. Zocher, M. Francke, and F. G. Rauscher, "Analysis of foveal characteristics and their asymmetries in the normal population," *Experimental Eye Research* **148**, 1–11 (2016).
 22. P. Scheibe, A. Lazareva, U.-D. Braumann, A. Reichenbach, P. Wiedemann, M. Francke, and F. G. Rauscher, "Parametric model for the 3d reconstruction of individual fovea shape from OCT data," *Experimental Eye Research* **119**, 19–26 (2014).
 23. M. A. Wilk, J. T. McAllister, R. F. Cooper, A. M. Dubis, T. N. Patitucci, P. Summerfelt, J. L. Anderson, K. E. Stepien, D. M. Costakos, T. B. Connor, Jr, W. J. Wiostko, P.-W. Chiang, A. Dubra, C. A. Curcio, M. H. Brilliant, C. G. Summers, and J. Carroll, "Relationship between foveal cone specialization and pit morphology in albinism foveal cone specialization and pit morphology," *Investigative Ophthalmology and Visual Science* **55**, 4186 (2014).
 24. L. Liu, W. Marsh-Tootle, E. N. Harb, W. Hou, Q. Zhang, H. A. Anderson, T. T. Norton, K. K. Weise, J. E. Gwiazda, L. Hyman, and the COMET Group, "A sloped piecemeal Gaussian model for characterising foveal pit shape," *Ophthalmic and Physiological Optics* **36**, 615–631 (2016).
 25. Y. Ding, B. Spund, S. Glazman, E. M. Shrier, S. Miri, I. Selesnick, and I. Bodis-Wollner, "Application of an oct data-based mathematical model of the foveal pit in parkinson disease," *Journal of Neural Transmission* **121**, 1367–1376 (2014).
 26. G. E. Farin, *Curves and Surfaces for Computer-Aided Geometric Design: A Practical Code* (Academic Press, Inc., Orlando, FL, USA, 1996), 4th ed.
 27. R. Ihaka and R. Gentleman, "R: A language for data analysis and graphics," *Journal of Computational and Graphical Statistics* **5**, 299–314 (1996).
 28. F. C. Oertel, H. Zimmermann, J. Mikolajczak, M. Weinhold, E. M. Kadas, T. Oberwahrenbrock, F. Pache, J. Bellmann-Strobl, K. Ruprecht, F. Paul, and A. U. Brandt, "Contribution of blood vessels to retinal nerve fiber layer thickness in nmosd," *Neurology - Neuroimmunology Neuroinflammation* **4** (2017).

1. Introduction

Optical coherence tomography (OCT) is a non-invasive imaging modality based on low-coherence interferometry [1]. OCT has become an essential diagnostic tool in ophthalmology for its capability to image the retina at micrometer resolution.

Recently, the scope of retinal OCT imaging has extended towards neurologic diseases. As part of the central nervous system, the retina comprises a similar cellular composition as the brain, and many neurologic disorders thus affect the retina. OCT is able to detect retinal

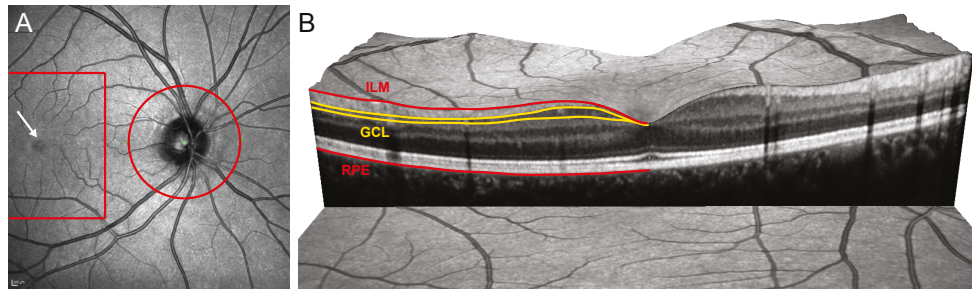


Fig. 1. Figure shows the structures of interest in the retina with layers ILM (Inner limiting membrane), GCL (Ganglion cell layer) and RPE (Retinal pigment epithelium layer).

changes in neurodegenerative disorders like Parkinson's disease [2] and cerebellar ataxias [3] as well as autoimmune neuroinflammatory disorders like clinically isolated syndrome [4], multiple sclerosis [5], MOG-ab-positive encephalomyelitis [6], and neuromyelitis optica spectrum disorders [7, 8].

Traditionally, OCT has been used to detect and describe macroscopic changes. However, neurologic diseases often lead to only small retinal changes, which rather need to be measured than can be seen directly. In the following, we will use the term *quantitative OCT* for this approach. Commonly, quantitative OCT determines the size of retinal structures as thickness or volume in a defined area of interest [9]. Structures of interest for measurements are the optic nerve head and the macula (Fig. 1). For example, one of the quantitative OCT parameters is the peripapillary retinal nerve fiber layer thickness (pRNFL), which is usually measured in a 12° ring scan around the optic nerve head. Quantitative measurements of macular changes were initially defined by, for example, total macular thickness (TMV) or total retinal thickness (TRT), which measure the full retinal thickness across the macula [9]. Recently, intra-retinal layer segmentation at the macula has been developed to allow quantification of intraretinal thickness or volume changes, for example, of the ganglion cell layer (GCL) [10–13].

Foveal shape analysis is a promising approach for quantitative OCT next to thickness or volume measurements. The few studies in this regard can be divided into two categories: data-driven, which directly employ segmentation lines from the OCT scan itself to compute various metrics, and model-driven, which use mathematical constructs to create a representation of the macula and fovea in order to calculate different features directly from the model.

Data-driven approaches All data-driven approaches known to the authors are based on the analysis of 2D images (B-scans) with results computed from one B-scan or averaged over two B-scans.

To analyze the variability of the healthy foveal shape and to investigate the relationship between this structure and the foveal avascular zone (FAZ), Tick et al. computed several parameters: pit depth, central foveal thickness, maximal retinal thickness, pit diameter, pit cross-sectional area, and the foveal inner retinal area. Using these parameters, the authors could show that the healthy foveal structure strongly correlates with its neurovascular structure [14].

Similarly, Chiu et al. introduced the parameters foveal photoreceptor thickness and foveal width, and found a large individual variation of FAZ size and shape in healthy retinæ and a negative correlation between FAZ diameter and foveal thickness [15].

Other studies investigated the way retinal structures change in the context of prematurity [16] or albinism [17] using fovea shape parameters like pit depth.

Model-driven approaches One of the first attempts to mathematically describe the foveal shape was published by Barak et al. [18]. Their approach employs an automated symbolic regression software that fits a section of the foveal profile around the center which was able to detect different patterns in the premacular hole foveal configurations and normal foveal configurations. A similar approach was used by Nesmith et al. to characterize changes that occur in the foveal anatomy with aging in a large number of OCT scans [19].

The first more general mathematical model was created by Dubis et al., who used Difference of Gaussians (DoG) function for a 2D fit of several radial scans passing through the lowest point of a macular scan [20]. The method derived three pit metrics (diameter, depth and slope) from a fitted model, which was symmetrical with respect to the fovea center. The model's symmetry was problematic, because of the fovea's asymmetry, which stems mostly from differences between the nasal and temporal retinal nerve fibers [14, 21]. The model was thus not accurate enough for modeling the asymmetric nature of the fovea and had problems covering the wide range of fovea shapes in the healthy population, due to other model fitting constraints, which were e.g. not able to model an extended flat part at the foveal pit in many healthy foveae [14, 21].

Scheibe et al. applied a different approach to overcome these drawbacks by creating a more flexible 2D model, which is fitted to each supporting direction in a circular region around the foveal center [22]. This method used a Gaussian like basis function ($\exp(-x^\gamma)$), when $\gamma = 2$, it would be a Gaussian basis function otherwise it would be an exponential function. The parameter γ defines the shape of the exponential basis function. The authors derived five parameters analytically: mean retinal thickness inside a radius of 1mm , foveal bowl area, retinal radius, and maximum height of the foveal rim. By applying this model to a large cohort of healthy subjects, the authors were able to confirm and further investigate the asymmetric nature of the fovea. Although, capable of modeling a large variety of data, and having a smaller root mean square error (RMSE) than previous approaches, the method has difficulties deriving 3D parameters such as volume due to the complexity of the computation because of the parameter γ . The RMSE is a standard metric to measure the model error. The low RMSE value indicates the high fidelity of a model.

Wilk et al. [23] used a similar algorithm described in [20] and applied it on a volume scan by extracting 180 radially oriented slices through the foveal center. In addition to the parameters defined in [20], the foveal pit volume was computed by calculating the space between the internal limiting membrane surface and the top of the foveal pit.

Liu et al. created a different 2D model, which uses a sloped piecemeal Gaussian function (SPG) to model the asymmetry and the foveal flatness [24]. The authors tested their method on a large number of macular scans and showed good RMSE compared to other 2D methods. The main drawback consists in the use of only two scans for each subject, a vertical and a horizontal one, which limits information on only these sections and prohibits generation of 3D metrics like volume.

Ding et al. developed an approach, which intends to model the surface of inner retinal layers using a 3D model-fit based DoG and a second order polynomial [25]. The authors used the model coefficients to discriminate between Parkinson patients and a control group. As a drawback, the model coefficients' relation to foveal shape itself is difficult to interpret. Additionally, although the model takes into account the difference in the slope for horizontal and vertical directions, it does not model the asymmetry in the anatomical ones (temporal-nasal), nor does it capture fovea shapes with very flat pits accurately.

Objective Against this background, the goal of this study was to develop a robust, model-driven 3D macula shape analysis method, which can be computed from standard macular volume OCT scans and from which foveal and macular shape metrics can be derived. In addition to available macular thickness measurements, our approach allows a detailed analysis of foveal

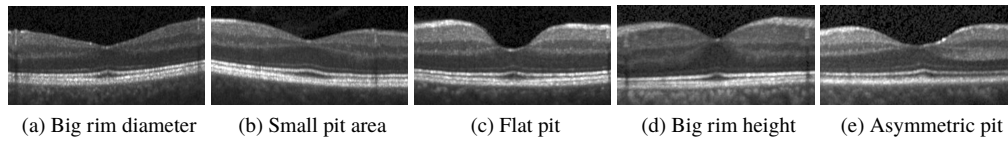


Fig. 2. Various shapes of the foveal pit

shape, including depth, diameter, slope, area and volume of different regions, as well as pit shape analysis.

2. Method theory

Most of the model driven state of art methods assume that the foveal pit shape is quite similar to the Gaussian function. Therefore, these methods use the Gaussian basis function for the mathematical modeling of the foveal pit [20, 22, 24, 25]. However, this assumption is not entirely true as we can see in Fig. 2 that the pit shape varies a lot from the Gaussian shape. Modeling the flatness of foveal pit is difficult with Gaussian basis function. The two regions of the Gaussian function (around and away from mean value) are dependent on each other and on the standard deviation of the given Gaussian function. However, the shape of the interior (pit area) and exterior (rim area) regions of fovea are independent of each other. For example, similar kinds of foveal pits can have significantly different rim heights. In summary, we can say that the Gaussian function is not an optimal basis function to describe macular and foveal shape.

To overcome these problems, we introduce a cubic Bézier based robust and flexible basis function, which is able to encounter all possible variations of the fovea shape. We fit the cubic Bézier polynomial in interior and exterior regions independently using a least square optimization with invariant features of fovea which will be discussed in the coming sections.

2.1. Invariant features of the fovea

Foveal shape in healthy population varies [21]. Figure 2, shows a selection of different foveal pit shapes from our cohort to exemplify this. In order to reconstruct all these variations, some invariant features of the shape are needed. Tangents at critical points of macula represent reliable and stable features. The critical points refer to the lowest point of the pit and the highest point around this region as shown in Fig. 3. The slope at these critical points is always zero and macula will have horizontal tangents at these points.

2.2. Cubic Bézier

Bézier curves were introduced by Dr. Pierre Bézier in early 1960s. A parametric Bézier curve of polynomial degree n is defined as:

$$Q(t) = \sum_{i=0}^n P_{i,n} B_{i,n}(t), \quad 0 \leq t \leq 1, \quad (1)$$

where the $P_{i,n}$ are the control points and $B_{i,n}$ are the Bernstein polynomials.

$$B_{i,n}(t) = \binom{n}{i} t^i (1-t)^{n-i}, \quad i = [0, 1, \dots, n]. \quad (2)$$

For a Bézier curve of degree n , there are $n + 1$ control points. From Eq. (1), one can see that the Bézier curve is a weighted average of control points where weights are defined using Bernstein

polynomials. For $n = 3$, Eq. (1) becomes the cubic Bézier equation:

$$Q(t) = \sum_{i=0}^3 P_i B_{i,3}(t), \quad 0 \leq t \leq 1. \quad (3)$$

Cubic Bézier curve will have four control points and is tangent to the first and last control points P_0 and P_3 respectively [26]. The relationship between control points, in terms of distance α , β and unit tangent directions T_{01} and T_{23} can be written as:

$$\begin{aligned} P_1 - P_0 &= \alpha \cdot T_{01}, \\ P_2 - P_3 &= -\beta \cdot T_{23}. \end{aligned} \quad (4)$$

Distance parameters α and β represent the distances between end control points (P_0, P_3) and inner control points (P_1, P_2) respectively. In our curve fitting algorithm, parameters α and β of each Bézier segment are used as shape parameters for an optimal curve fitting. The direction of a Bézier curve at its endpoints is uniquely determined by the tangent vector. Thus, by choosing the same tangent vector for two adjacent Bézier segments tangent continuity (geometrical continuity G^1) at each junction is assured, and thus throughout the whole composite spline curve.

2.3. Least squares optimization

A least squares fitting approach is applied for each B-scan/radial scan using a cubic Bézier curve and tangents at critical points, which are derived from the invariant features of the macular shape. Let us consider $c(x)$ as a central B-scan, which contains the minimal retinal thickness point as shown in Fig. 3(a).

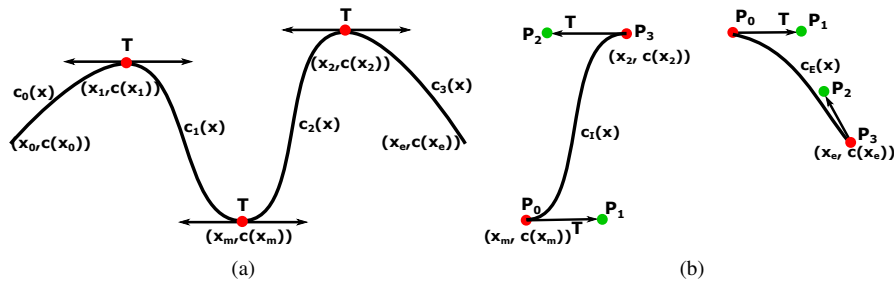


Fig. 3. (a) The central B-scan of a volume with invariant tangent at critical points. Red dots = critical points. (b) The interior and the exterior segment of the corresponding right half of the B-scan. The inner (P_1, P_2) and end (P_0, P_3) control points are shown in green and red, respectively.

The central B-scan can then be decomposed into two interior ($c_1(x), c_2(x)$) and two exterior ($c_0(x), c_3(x)$) segments, where the right half of the central B-scan is defined as the segment between the points $(x_m, c(x_m))$ and $(x_e, c(x_e))$ as shown in Fig. 3(a). The maximum point of the right half of the central B-scan can be computed, as represented by $(x_2, c(x_2))$. Two segments can be made using the critical point $(x_2, c(x_2))$ and each segment was denoted as $c_I : [x_m, x_2] \rightarrow \mathbb{R}$ for the interior, and $c_E : [x_2, x_e] \rightarrow \mathbb{R}$ for the exterior segment as shown in Fig. 3(b).

For interior segment (c_I), end points, P_0 and P_3 , have horizontal tangent lines $T = [1, 0]$ and inner control points, P_1 and P_2 , which are lying opposite to each other w.r.t. their tangent direction, as shown in Fig. 3(b). Thus, Eq. (4) can be modified to give:

$$\begin{aligned} P_1 &= P_0 + \alpha \cdot T, \\ P_2 &= P_3 - \beta \cdot T. \end{aligned} \quad (5)$$

For the exterior segment (c_E), only one of the end points has a horizontal tangent and one of the inner control points (P_1) lies in the same horizontal tangent direction. Equation (4) for exterior segments then becomes:

$$P_1 = P_0 + \alpha \cdot T. \quad (6)$$

The other inner control point, P_2 , for the exterior segment does not have a horizontal tangent direction ($T = [1, 0]$); therefore the value of P_2 is optimized without using any invariant feature of the macula. In this proposed method, control points P_i are defined in \mathbb{R}^2 space.

Next, the optimized values of α and β are computed to achieve the best-fit cubic Bézier for each segment of the scan. The optimization process begins from the interior segment. By using Eq. (3) and 5, the cubic Bézier equation for interior segment (c_I) can be modified as follows:

$$Q_I(t, \alpha, \beta) = \alpha T B_1(t) - \beta T B_2(t) + P_0(B_0(t) + B_1(t)) + P_3(B_2(t) + B_3(t)). \quad (7)$$

If the corresponding segment has m data points and is represented by D^I then the least squares energy function can be expressed as:

$$E(t, \alpha, \beta) = \sum_{i=1}^m \|D_i^I - Q_I(t_i, \alpha, \beta)\|^2, \quad (8)$$

where t_i represents discrete values of t corresponding to the data points D_i^I and it is computed using the uniform parametrization ($t_i = i/m \quad \forall i \in [0, 1, \dots, m]$). Equation (8) shows a quadratic energy function in α and β for a given parametric value of t and higher order polynomial in t for a given α and β . The minimization of the above energy function then becomes a multi-space optimization, since there are three different variables to be minimized. The multi-space optimization procedure for t , α and β occurs using the following steps:

1. First, Eq. (8) is a quadratic energy function in α and β for a given t , so it can be solved by using the linear system of equations. An initial value is given to $t \in [0, 1/m, 2/m, \dots, 1]$ using the uniform parametrization and corresponding α and β values are calculated by computing the first derivative of the given energy function w.r.t. α and β .

$$\nabla_{\alpha} E = 0, \quad \nabla_{\beta} E = 0. \quad (9)$$

To compute the gradient of the given energy in terms of α :

$$\nabla_{\alpha} E = 2 \sum_{i=1}^m (D_i^I - Q_I(t_i, \alpha, \beta)) \cdot B_1(t_i) \cdot T. \quad (10)$$

By using Eq. (9), we can conclude by stating the following relation:

$$\sum_{i=1}^m B_1(t_i) \cdot Q_I(t_i, \alpha, \beta) = \sum_{i=1}^m D_i^I \cdot B_1(t_i), \quad (11)$$

where the left hand side of Eq. (11) shows only α as an unknown variable, since the terms of β are omitted due to differential operations. However, β can also be computed using Eq.(9) in the same manner.

2. Second, the optimized value of t is calculated using the gradient descent method with the values for α and β that were computed in the previous step.

$$\nabla_t E = 0. \quad (12)$$

Similar to Eq. (10), the derivative of the given energy function w.r.t t is computed as follows:

$$\nabla_t E = -2 \sum_{i=1}^m (D_i^I - Q_I(t_i, \alpha, \beta)) \cdot Q_I'(t_i, \alpha, \beta), \quad (13)$$

where $Q_I'(t_i, \alpha, \beta)$ represents the first derivative of cubic Bézier in terms of t . The optimized value of t is computed using the following equation:

$$\tilde{t}_i = t_i + s \cdot \nabla_t E, \quad (14)$$

where s represents the step size of the gradient descent method and \tilde{t}_i is the optimized value of t . In the next iteration, \tilde{t}_i will be used as the initial value of t to compute the new α and β . Throughout the whole experimentation the step size was fixed to $s = 0.1$.

These two steps are iterated until the stable minimum of the energy function in Eq. (8) is obtained. Equation (13) depends not only on t but also on α, β , thus allowing stable minimum to be reached. The minimum of the given energy can be achieved in 400 iterations. After 400 iterations, there is no significant change in the optimization result.

For the exterior segment (c_E), our optimization procedure is different compared to the interior segments as only one end point has a horizontal tangent. Using Eq. (6) and Eq. (3), we can have a modified equation for optimization:

$$Q_E(t, P_2, \alpha) = \alpha T B_1(t) + P_0(B_0(t) + B_1(t)) + P_2 B_2(t) + P_3 B_3(t). \quad (15)$$

Similar to the energy function in Eq. (8), here we have an energy function, which depends on t, P_2 and α and which is defined as:

$$E(t, P_2, \alpha) = \sum_{i=1}^m \|D_i^E - Q_E(t_i, P_2, \alpha)\|^2, \quad (16)$$

where D^E represents data points corresponding to the external segment. The minimization of this given function is performed in a similar fashion as the interior segment parameter optimization. First, the derivative of the energy function w.r.t P_2 and α , for a given initial uniform parameterized t , is computed. Then, the optimized t with newly obtained values for P_2 and α is determined.

3. Materials and methods

To evaluate the proposed method macular volume scan ($25^\circ \times 30^\circ$, 61 vertical or horizontal B-scans, 768 A-scans per B-scan, with each B-scan being the result of 9-15 averaged B-scans) captured with Spectralis OCT (Heidelberg Engineering, Heidelberg, Germany) were used. The voxel dimensions in horizontal and, axial directions and distance between B-scans in this data set were approximately 11.69, 3.87, and $125 \mu\text{m}$ respectively. A total of 187 OCT scans, 95 from healthy controls (HC) and 92 from patients with different autoimmune neuroinflammatory diseases, were selected from the NeuroCure Clinical Research Centers' imaging database. All scans underwent quality control by an experienced rater. Automatic layer segmentation was performed with the device's software (Eye Explorer 1.9.10.0 with viewing module 6.0.9.0). The institute's imaging database only contains images derived from local studies that were approved by the local ethics committee at the Charité - Universitätsmedizin Berlin and were conducted following the Declaration of Helsinki in its currently applicable version.

All computations were carried out using MATLAB 2016b (MathWorks, Inc., Natick, MA, USA). The statistical analysis was conducted using R version 3.3.2 [27]. ICC (inter class correlation) and GEE (Generalized estimating equation) were used for statistical measurements. The ICC measures the repeatability of the proposed parameters and GEE (p-value) shows the significance between the two groups of data for each of the proposed parameters.

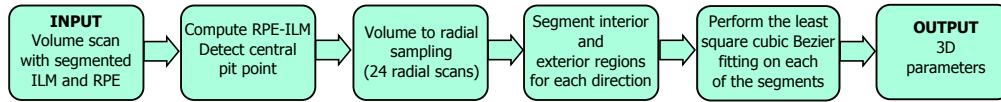


Fig. 4. The pipeline of the proposed algorithm.

3.1. Method pipeline

Figure 4 shows the pipeline of our algorithm. In order to import data into MATLAB, Heidelberg Spectralis OCT raw data format was exported from the device. This data contains additional to the image information, the coordinates of the inner limiting membrane (ILM) and the lower boundary of the retinal pigment epithelium layer denoted throughout our paper for simplicity reasons as RPE. The whole algorithm is implemented in the following steps:

1. **ILM-RPE Computation and Minimal Foveal Point Detection:** In the first step, the height difference between the ILM and the RPE of each volume scan is extracted. This represents the macular thickness surface. Using this difference has the advantage of removing the slant of the scan created at the measurement and/or by the curved shape of the eye. Let us consider a volume scan and the corresponding thickness profile represented as the graph function $\mathcal{M} : (x, y) \rightarrow \mathbb{R}$, where $(x, y) \in \Omega$ and Ω represents our region of interest. A volume scan is the combination of A-scans and B-scans obtained from the OCT scanner. We assume that x and y represent A-scans and B-scans directions respectively.

To determine the fovea's center, a region Ω of 1 mm radius is taken from the surface centered at the fovea automatically detected by the OCT device. The information about this center point is included in the raw data export. In order to detect the lowest point of foveal surface, we look at the minima of this region.

$$\mathcal{M}_m = \mathcal{M}(x_m, y_m), \quad (17)$$

where x_m, y_m are the coordinate of the minimum value \mathcal{M}_m of the volume scan. If several minimas are detected, then the median point of them is taken as the center of foveal pit.

2. **Volume to Radial Sampling:** This is the second step of the proposed method as shown in Fig. 4. For 3D shape analysis of fovea, information from the whole volume is needed, and therefore the scan is re-sampled into a radial one. The radial scans capture the foveal pit shape accurately as they have more samples near the center compared to the outer region. Sampling from volume \mathcal{M} to radial \mathcal{M}_p can be done in the following steps:

- (a) Create a polar grid $\mathcal{M}_p(r, \theta)$, centered at (x_m, y_m) with zero height value. Radius and angle between the radial lines will be defined by the user.
- (b) Compute the height value of $\mathcal{M}_p(r, \theta)$ using bilinear interpolation between the nearest four points of the $\mathcal{M}(x, y)$ which are closest to the corresponding (r, θ) .
- (c) Now, there are $n = (2\pi/\theta)$ radial scans represented as:

$$c(r, \theta_i) \in \mathcal{M}_p(r, \theta) \quad \text{where} \quad i = 1, \dots, n.$$

These radial scans approximate the original volume scan as shown in Fig. 5(a).

In our experimentation, we choose $r = 2\text{mm}$ and $\theta = 15^\circ$ for radial sampling.

3. **Segmentation of the Radial Scans:** Each of the radial scans $c(r, \theta_i)$ is segmented into interior c_I and exterior c_E regions at corresponding maximum (critical) point, as shown in Fig. 3(b).

4. **Cubic Bézier Fitting using Least Square Optimization:** For each of the segments of the radial scan, a cubic Bézier with least square optimization as explained in section 2.3 is fitted. For the interior segment, Eq. (8), (9) and (12) is used to compute optimized α , β and t . Then, the interior segment using the optimized parameters is reconstructed by assigning these to Eq. (7). Similarly, for exterior segment, Eq. (16) is used and optimized α , P_2 are computed. Then the exterior segment is reconstructed by using Eq. (15). To get a complete 3D parameterized modeling of the fovea, a cubic Bézier has to be fitted to each of the re-sampled radial scans. Figure 5(b) shows the 3D parameterized model with 24 radial scans.

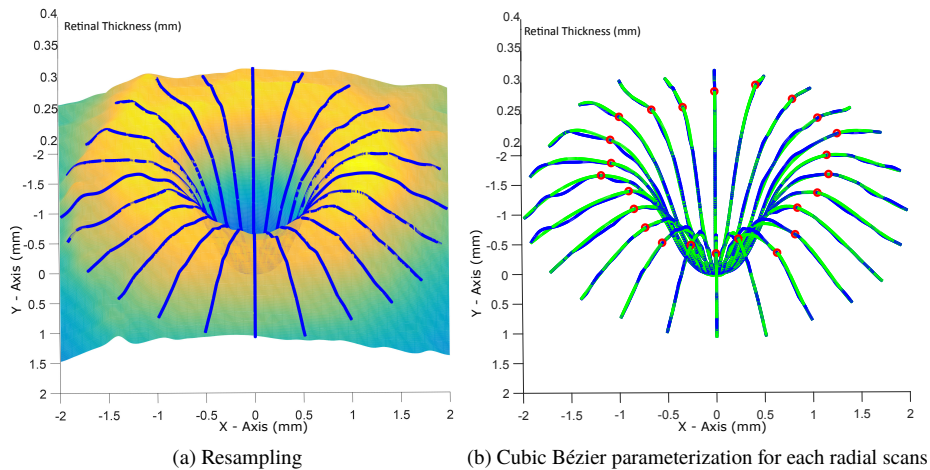


Fig. 5. 3D shape reconstruction procedure. (a) Shows a volume scan with 61 B-scans and 768 A-scans and corresponding 24 radial directions (blue) using the bilinear interpolation. (b) Represents the 24 fitted radial scans (green) using the least square optimization. The red points show the critical points for each radial scan.

5. **Parameters Computation:** This is the last step of the algorithm. Now, we have a cubic Bézier parameterized 3D radial scans of a volume scan. By using this parameterization, several parameters for the volume scan are computed. The analytical formulations of these parameters are shown in the next section.

4. Parameters

In this section, we present several shape parameters for a volume scan using a cubic Bézier parameterization. Rim point of a radial scan is defined as the maximum height point in the corresponding radial scan. Let us consider that there are n number of radial scans re-sampled from a volume scan and $(p_1, p_2, \dots, p_n) \in \mathbb{R}^3$ are the corresponding rim points. Figure 6 shows re-sampled radial scans from a volume scan divided into two parts: $c(r, \theta_i)$ and $c(r, \theta_i + \pi)$. The notation used to denote the corresponding least square optimization fitted radial scan parts is $Q(t, \theta_i)$ and $Q(t, \theta_i + \pi)$ for all $i = 1, \dots, n$. A visual representation of some of the 3D parameters is shown in Fig. 8 and 9. Figure 7 shows two parameterized radial scans ($Q(t, \theta_i)$ and $Q(t, \theta_i + \pi)$) of a volume scan which differ by the angle π . Several basic parameters are defined based on these two radial scans. Q_I and Q_E represent parameterized interior and exterior segments respectively. Most of the 3D parameters are computed by first computing the values for each radial scans and then taking the average over these scans.

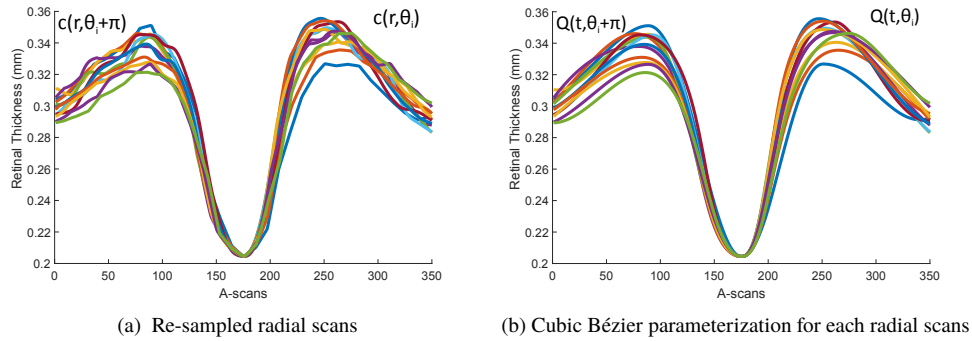


Fig. 6. 2D shape reconstruction (a) Shows re-sampled radial scans from a volume scan divided in two parts: $c(r, \theta_i)$ and $c(r, \theta_i + \pi)$ (b) Shows corresponding fitted radial scans using least square optimization. These are represented by $Q(t, \theta_i)$ and $Q(t, \theta_i + \pi)$ and $i = 1, \dots, n$. A full radial scan can be consider as a combination of $c(r, \theta_i)$ and $c(r, \theta_i + \pi)$ and is shown in different colors and corresponding parametrized curves are shown in the same color.

Central Foveal Thickness (h_{cft}): refers to the central foveal thickness which is defined as the minimum height of fovea at the center of the pit. From Eq. (17), h_{cft} can be written as:

$$h_{cft} = \mathcal{M}(x_m, y_m). \quad (18)$$

The h_{cft} of each radial scan is the same because (x_m, y_m) is the center of radial and represents the beginning as well as the lowest point for each radial scan.

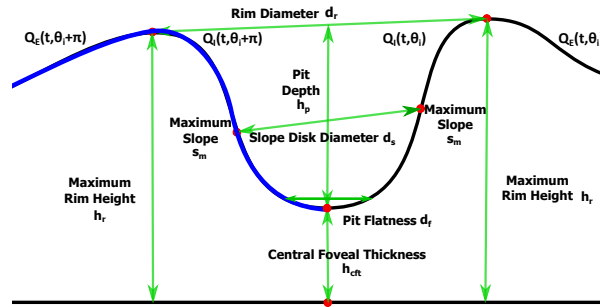


Fig. 7. Visualization of 2D parameters on the central B-scan.

Average Rim Height (h_r): is defined as average of maximum height in each radial scan of a volume (as shown in Fig. 3). Average rim height is written as:

$$h_r = \frac{1}{n} \sum_{i=1}^n \max(c(r, \theta_i)). \quad (19)$$

Rim Disk Area (A_r): To compute the rim disk area, the normal to the disk plane is calculated as shown in Fig. 8. The covariance analysis of all the rim points provides not only the disk normal

but also shape information as described below. Rim points covariance matrix can be computed as:

$$C_r = \frac{1}{n} \sum_{i=1}^n (p_c - p_i)^T (p_c - p_i),$$

$$p_c = \frac{1}{n} \sum_{i=1}^n p_i.$$
(20)

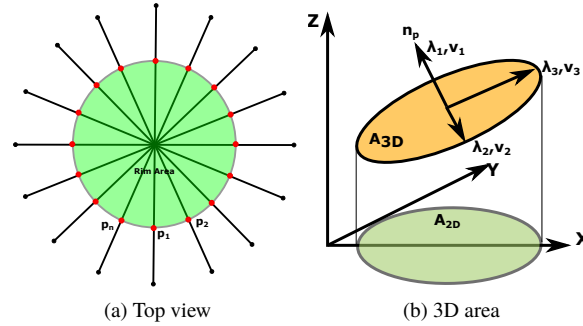


Fig. 8. a: Top view of rim disk. b: Normal vector of rim disk plane and corresponding covariance eigenvalues and eigenvectors.

Eigen analysis of matrix C_r provides shape information about the rim disk. Let us consider the vector $\lambda = [\lambda_1, \lambda_2, \lambda_3]$ representing the eigenvalues sorted in decreasing order: $\lambda_1 \geq \lambda_2 \geq \lambda_3$ and $[v_1, v_2, v_3]$ are the corresponding eigenvectors. The most dominant eigenvalues λ_1 and λ_2 represent **Major** and **Minor** axis of the rim disk respectively. The least dominant eigen direction will be the disk normal so $n_p = v_3$. Now, **Rim Disk Area** can be computed as:

$$A_{3D} = \frac{A_{2D}}{\cos\theta}, \quad \theta = \angle(n_p, n_z),$$
(21)

where $n_z = [0, 0, 1]$ and $A_{2D} : \mathbb{R}^2 \rightarrow \mathbb{R}$ is the area of the projection of A_{3D} on XY-plane.

Average Rim Disk Diameter (d_r): Let us consider p_{θ_i} and $p_{\theta_i+\pi}$ are two rim points corresponding to two parameterized opposite radial scans($Q(t, \theta_i)$ and $Q(t, \theta_i + \pi)$) then average rim diameter is written as:

$$d_r = \frac{2}{n} \sum_{i=1}^{n/2} \|p_{\theta_i} - p_{\theta_i+\pi}\|.$$
(22)

Average Pit Depth (h_p): represents the depth of foveal pit and can be computed as the difference between the average rim height and central foveal thickness:

$$h_p = h_r - h_{cft}.$$
(23)

Average Maximum Pit Slope (s_m): Average maximum pit slope measures the steepness of foveal pit. It is defined as the average of the maximal slope of each radial scan. The slope of a parameterized radial scan $Q(r, \theta_i)$ is defined as:

$$s_i = \frac{dQ_i^y(t)/dt}{dQ_i^x(t)/dt} \quad i = 1, \dots, n,$$

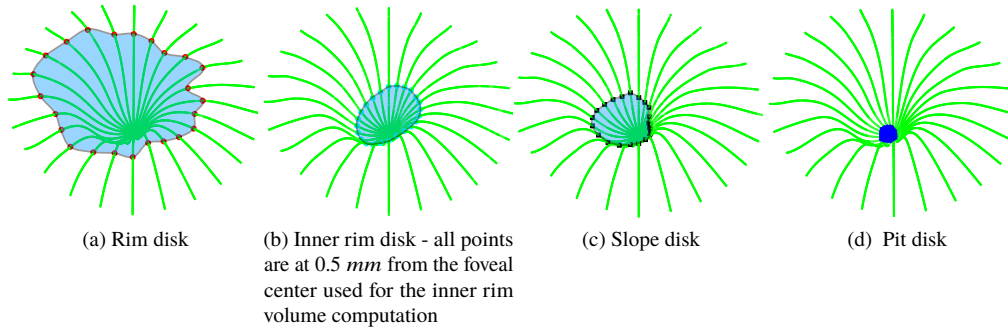


Fig. 9. A visual representation of the 3D parameters. The rim and the inner rim volume is defined as the volume covered by the corresponding disk area. The radius for the inner disk area and the volume is defined by user.

where $Q_I^y(t)$ and $Q_I^x(t)$ represent parameterized x and y coordinates for the interior segment. To calculate the maxima of the above equation, the gradient, $\nabla_t s_i = 0$ is computed. This gives the value of t_{m_i} for the maximal slope (s_{m_i}):

$$s_{m_i} = -\frac{P_3^y - P_0^y}{\alpha - \beta - \sqrt{\alpha\beta} - (P_3^x - P_0^x)},$$

$$t_{m_i} = \frac{\sqrt{\alpha}}{\sqrt{\alpha} + \sqrt{\beta}},$$
(24)

where P_3^y and P_0^y are the y coordinates of the end control points of $Q_I(t, \theta_i)$. Similarly, P_3^x and P_0^x are the x coordinates of the end control points of $Q_I(t, \theta_i)$. Average maximum pit slope of a volume is defined as:

$$s_m = \frac{1}{n} \sum_i^n s_{m_i}. \quad (25)$$

Average Slope Disk Diameter (d_s): Average slope disk diameter is computed similar to average rim diameter d_r . Slope width is computed between two opposite parameterized radial scans: $Q(t, \theta_i)$ and $Q(t, \theta_i + \pi)$ and the corresponding maximum slope points are $p_{\theta_i}^s$ and $p_{\theta_i + \pi}^s$ such that:

$$\begin{aligned} p_{\theta_i}^s(x) &= Q^x(t_m, \theta_i), \\ p_{\theta_i}^s(y) &= Q^y(t_m, \theta_i), \\ p_{\theta_i + \pi}^s(x) &= Q^x(t_m, \theta_i + \pi), \\ p_{\theta_i + \pi}^s(y) &= Q^y(t_m, \theta_i + \pi), \end{aligned} \quad (26)$$

where t_m represents maximum slope point in parametric domain as shown in Eq. (24) and $Q^x(t_m, \theta_i)$, $Q^y(t_m, \theta_i)$ are the corresponding x and y coordinate. Average slope width of a volume is defined as:

$$d_s = \frac{2}{n} \sum_{i=1}^{n/2} \|p_{\theta_i}^s - p_{\theta_i + \pi}^s\|. \quad (27)$$

Slope Disk Area (A_s): Slope disk area can be computed similar to the rim disk area. Let us consider $(p_1^s, p_2^s, \dots, p_n^s) \in \mathbb{R}^3$ are maximum slope points corresponding to each radial scan and are computed using Eq. (24) and (26). Covariance of maximal slope points can be computed

using Eq. (20) to obtain the normal vector, major and minor axes of the slope disk.

Pit Flat Disk Area (A_f): Pit flat disk area measures the flatness of foveal pit around the center and is computed using a threshold value τ for each of radial scan. In each radial scan, a point $p_{\theta_i}^f$ where retinal thickness is smaller than τ is computed. Then the corresponding segment from center (x_m, y_m) to the computed point $p_{\theta_i}^f$ is treated as flat. This can be done in following two steps:

1. First of all, the parametric value t_f corresponding to threshold value τ is calculated:

$$\tau - Q_I^y(t_f, \theta_i) = 0. \quad (28)$$

2. Now, the x value corresponding the parameterized value t_f is computed:

$$d_{f_i} = Q_E^x(t_f, \theta_i). \quad (29)$$

Point $p_{\theta_i}^f = (d_{s_i}, \tau, \theta_i)$ corresponds to the pit flat point for a single radial scan. Similarly, let us consider $(p_1^f, p_2^f, \dots, p_n^f) \in \mathbb{R}^3$ as pit flat points. The area, major and minor axis of the pit flat disk can be computed similar to rim disk area.

Average Pit Flat Disk Diameter (d_f) is computed using d_{f_i} from Eq. (29):

$$d_f = \frac{2}{n} \sum_{i=1}^n d_{f_i}. \quad (30)$$

Rim Volume (V_r): In general, the volume under a surface in Cartesian and Polar domains and can be computed using the following equation:

$$V_r = \iint_A f(x, y) dx dy = \int_0^{2\pi} \int_0^R c(r, \theta) r dr d\theta.$$

After the discretization process of the whole volume into n radial directions, the above equation will become:

$$V_r = \frac{2\pi}{n} \sum_{i=1}^n \int_0^R c(r, \theta_i) r dr.$$

The above equation is modified using the following substitution. The interior parameterized curve $Q_I(t, \theta_i)$ is defined between center and rim points. So the parametric value $t \rightarrow \{Q_I^x(t, \theta_i), Q_I^y(t, \theta_i)\}$ is $t = 0$ and $t = 1$ at center and rim points respectively. Similarly, $r = Q_I^x(t, \theta_i)$, $R = Q_I^x(1, \theta_i)$, $c(r, \theta_i) = Q_I^y(t, \theta_i)$ and $dr = \frac{dQ_I^x(t, \theta_i)}{dt} dt$. After the substitution, rim volume can be written as:

$$V_r = \frac{2\pi}{n} \sum_{i=1}^n \int_0^1 Q_I^y(t, \theta_i) Q_I^x(t, \theta_i) \frac{dQ_I^x(t, \theta_i)}{dt} dt. \quad (31)$$

In the above equation, $R = P_3^x$ and at end point of the parametric curve t is equal to 1. R might have different values for different radial scans because of asymmetry of foveal pit.

Inner Rim Volume (V_{IR}): Is defined as the volume of fovea within a fixed radius from center. The radius is given by the user. Let us consider t_u to be the parametric value corresponding to the user input radius r_u for each radial direction. Now, Eq. (31) can be modified as follows:

$$V_{IR} = \frac{2\pi}{n} \sum_{i=1}^n \int_0^{t_u} Q_I^y(t, \theta_i) Q_I^x(t, \theta_i) \frac{dQ_I^x(t, \theta_i)}{dt} dt. \quad (32)$$

Before using the above equation, it has to be tested whether radius R will be equal to the minimum of P_3^x from all radial directions. In case that R is bigger than any of P_3^x , the exterior segment has to be introduced into the integration as well.

Pit Volume (V_p): The total volume (V_t) under the rim disk is calculated, $V_t = A_{3D}h$, where h is the average height of rim points. Then the pit volume can be defined as:

$$V_p = V_t - V_r. \quad (33)$$

Table 1. Repeatability test for the 3D parameters. Abbreviations: ICC - intra-class correlation coefficient, LCI - lower confidence interval and UCI - upper confidence interval.

Parameters	ICC	LCI	UCI
Avg. Pit Depth (h_p) (mm)	0.981	0.966	0.990
Central Foveal Thickness (h_{cft}) (mm)	0.989	0.980	0.994
Avg. Rim Height (h_r) (mm)	0.976	0.957	0.987
Avg. Rim Disk Diameter (d_r) (mm)	0.925	0.868	0.960
Rim Disk Area (A_r) (mm ²)	0.919	0.858	0.957
Major Axis Rim Disk (λ_3^r) (mm)	0.909	0.843	0.952
Minor Axis Rim Disk (λ_2^r) (mm)	0.906	0.838	0.950
Avg. Slope Disk Diameter (d_s) (mm)	0.930	0.878	0.963
Slope Disk Area (A_s) (mm ²)	0.946	0.905	0.972
Major Axis Slope Disk (λ_3^s) (mm)	0.936	0.888	0.966
Minor Axis Slope Disk (λ_2^s) (mm)	0.946	0.905	0.972
Avg. Pit Flat Disk Diameter (d_f) (mm)	0.896	0.821	0.945
Pit Flat Disk Area (A_f) (mm ²)	0.915	0.852	0.955
Major Pit Flat Disk Length (λ_3^f) (mm)	0.899	0.825	0.946
Minor Pit Flat Disk Length (λ_2^f) (mm)	0.913	0.849	0.954
Rim Volume (V_r) (mm ³)	0.895	0.820	0.944
Inner Rim Volume (V_{IR}) (mm ³)	0.966	0.940	0.983
Pit Volume (V_p) (mm ³)	0.960	0.929	0.979
Avg. Max. Pit Slope (s_m) (Degrees)	0.969	0.945	0.984
α_m (mm)	0.917	0.855	0.956
β_m (mm)	0.810	0.686	0.896

5. Experiments, results and discussion

Scans from 187 eyes consisting of 95 healthy eyes and 92 eyes from patients with autoimmune neuroinflammatory diseases (with and without previous optic neuritis) were processed. Our implementation is quite straight forward and follows the pipeline mentioned in section 3.1. The proposed algorithm is implemented in a single computation thread and it takes around 3 seconds to compute the parametric 3D model and related parameters.

5.1. Re-test reliability

The proposed algorithm was able to successfully model all the scans; visual inspection of model results did not suggest modelling failure in any of the included scans. Table 1 shows the test-retest reliability applied to a group of data including three repeated measurements of 30 healthy eyes. Intra-class correlation coefficient (ICC) for the 3D derived parameters varied from 0.8102 for β_m to 0.9894 for the Central foveal thickness as shown in Table 1. From Table 1, parameter β_m has the lowest repeatability. Basically, α_m and β_m are the average of all α and β belonging to radial

scans of interior region of fovea. As mentioned in Eq. (5), α and β represent the distance between control points P_0, P_1 and P_3, P_2 respectively. The lowest ICC value obtained for β_m indicates that the distance between the P_3 and P_2 is not consistent. Perhaps, the small inaccuracy in rim point detection is leading to the low repeatability of the β_m . On the other hand, α depends on center or beginning control point (P_0) which is fix for a volume scan. Therefore, α_m has a better repeatability compared to β_m .

5.2. Model accuracy

For root-mean-square-error (RMSE) comparison, we have implemented two state-of-the-art methods for foveal shape analysis, the one proposed by Ding et al. [25], and the one described in Dubis et al. [20] and compared them with our method. For a better readability, we renamed [25] as M_1 and [20] as M_2 . In case of M_1 the 3D approach was implemented, as presented in the paper [25]. For M_2 the 3D version was modeled by extending the 2D method presented by the authors on our radial re-sampled volume. In order to visualize the behaviour of M_1 vs. M_2 vs. CuBe, we present fitting results on the central B-scan for the same subject in Fig. 10. As shown in the figure, CuBe is able to capture the exact foveal shape with the lowest RMSE compared to methods M_1 and M_2 .

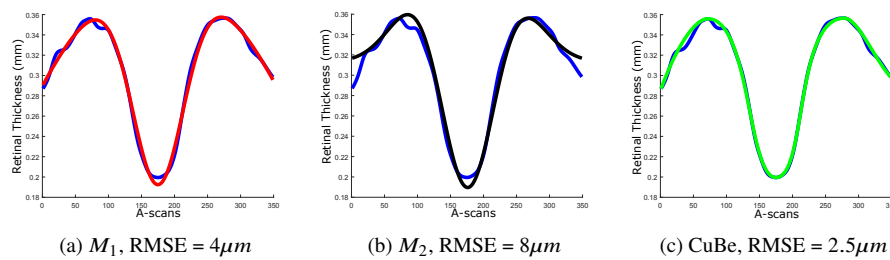


Fig. 10. Comparison of the proposed method with two state-of-the-art methods [25] and [20]. Blue curve is the raw input (ILM-RPE difference) at the central B-scan and black, red and green are the reconstructed curves with [20], [25] and our method (CuBe) respectively. The RMSE values show that the proposed method manages to reconstruct the shape with minimum artifacts, specifically the pit shape.

Methods M_1 and M_2 , both are using Gaussian-based basis function to model foveal shape. The method M_2 [20] uses DoG (difference of Gaussian) as basis function for each radial scan and derives only three parameters (slope, rim diameter and rim height) to characterize the shape of the fovea, which is a too small number to encounter all the variation of the fovea shape. The optimization procedure of the mentioned energy function in this method is complex because of the two different Gaussian basis and the energy function can have unstable minima quite often. The method M_1 [25] applies a Gaussian along with a quadratic and linear basis function to produce a 3D model of a volume scan. It needs eight parameters ($A_0, A_{11}, \dots, A_{22}$) to reconstruct a 3D model of a volume scan. However, these parameters do not represent any morphological information of the fovea, which makes their interpretation in relation to morphological characteristics rather difficult. Scheibe et al. introduced a stable and accurate modeling of the fovea using double derivative of an exponential function [22]. This method [22] is applied to re-sampled radial scans from 3D macula cube scans. There are four parameters used to parametrize a radial scan. However, the parameter γ in the exponential basis function ($\exp(-x^\gamma)$) [22]) makes the algorithm more complex and leads to difficulties in optimization and analytical analyses. Additionally, direct analytical derivation of 3D parameters, e.g. volumes presents several computational problems. Recently, Liu et.al [24] has introduced a sloped piecemeal Gaussian model for characterizing

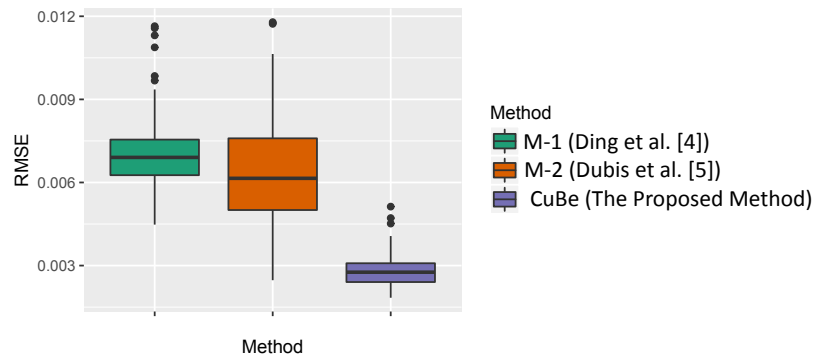


Fig. 11. RMSE values for 3D M_1 , M_2 , and $CuBe$ for the whole data set.

foveal pit shape. This method uses a combination of linear and Gaussian basis function along with an additional parameter which encounters the pit bottom flatness. As this method is using piecewise basis function, the optimization process is not straight forward. However, this method only characterizes the foveal pit and not the complete fovea shape.

In Fig. 11, we show different RMSE values for 3D fitting on a volume scan. These RMSE values are computed between raw ILM-RPE segmented data (as mentioned in section 3.1) from Heidelberg Spectralis OCT and the corresponding fitted model. The comparison has been performed between the proposed method, $CuBe$ and methods M_1 , M_2 . The RMSE values for our approach show overall lower values compared to other methods, as our method reconstructs the foveal pit more accurately as shown in Fig. 10. In the proposed method, the highest RMSE occurs in regions where the segmentation is mostly influenced by blood vessels. These blood vessels produce several "jumps" spatially close to each other as shown in Fig. 12 (bottom). These "jumps" have a strong influence also in the detection of maximum height points (rim points) which can lead to a higher RMSE because our parametrization scheme depends on these critical points. In such cases, peaks are representing the vessels and not the retinal tissue, which might induce an additional noise when investigating differences between healthy and pathological data [28].

An important aspect of the presented method is the ability to utilize characteristic fovea properties for the whole circular region (re-sampled radial region) because of the flexible and robust cubic Bezier parametrization scheme. This implies that we derive the discussed 3D parameters in a completely new fashion. This gives us the possibility to explore new morphological features of fovea in terms of Rim Disk, Slope Disk, and Pit Flat Disk by looking at the eigenvectors of the covariance matrix defined in Eq. (20). By computing pit flatness and its area from the 3D reconstruction, we are able to provide not only a better visual insight of this region but also a potentially new diagnostic parameter for further investigations into several diseases e.g. those characterized by nerve fibers and ganglion cells loss [4, 7, 8]. Another beneficial aspect of the presented 3D approach is in the flexibility of defining the foveal radius. This can be computed from the model itself as a specific feature of each radial Bézier curve part, and as such it would take into account the asymmetric nature of this region, or as a variable radius, defined by the user.

5.3. Application in HC and patients with autoimmune neuroinflammatory disorders

Having all the parameters described in the previous section, a first analysis of the morphological aspects of the data set can be performed. Table 2 shows all the 3D parameters defined for the HC and patient groups. The measurements obtained with our method have similar values to the ones encountered in literature. For characteristics like Rim Disk Area, Slope Disk Area, Pit Flat Disk

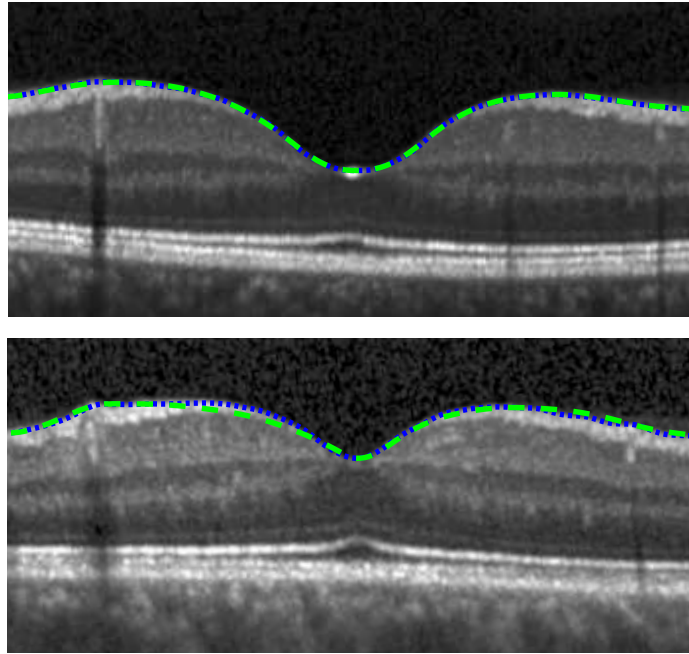


Fig. 12. Two examples of 2D curve fitting results with the lowest (top) and the highest (bottom) RMSE values selected from the entire data set analyzed. Original data is shown in blue and fitted curve in green. RMSE values are from top to bottom, $1.0 \mu\text{m}$, $7.1 \mu\text{m}$.

Area a comparison to existing literature was not possible since this is the first time that these parameters have been introduced.

We also investigated the capability of the derived parameters to differentiate between HC and patients. To this end GEE analyses was performed. Table 2 presents that several parameters show significant differences between HC and patients. These results open new possibilities for further investigation of fovea shape derived parameters in more specific clinical diseases.

6. Conclusion

In summary, we have developed a reliable, accurate and meaningful approach for fovea shape analysis, which is able to correctly model the profile of the foveal region and reconstruct its 3D shape. Our method has been shown to robustly encounter possible variations in foveal shape in HC but also in foveas that undergo considerable changes during the course of a neuroinflammatory disease.

The mathematical model created is simple and has the advantage of a straight forward derivation of parameters. The computed parameters are in direct relation to the geometry modeled, and therefore provide an intuitive way of interpretation for further medical analysis and clinical interpretation. A major advancement of the developed method is that it is possible to analyze the foveal shape in a clinical context, especially from the 3D perspective.

Several derived foveal shape parameters showed statistically, significant differences between HC and patients with neuroinflammatory diseases of the central nervous system and could potentially reveal more insights into the foveal morphology and the changes it undergoes especially when correlated with other clinical information. Further applications in ophthalmologic diseases like macular degeneration are worth to be investigated as well.

Table 2. Analysis of all the 3D parameters defined for the HC and patient group. The last column shows the GEE analysis between the two groups. Abbreviations: HC - healthy controls. SD - standard deviation, Min - minimum value, Max - maximum value, GEE - generalized estimating equation models analysis accounting for the inter-eye/intra-subject dependencies, p - p value

Parameters	HC		Patients		GEE
	Mean (SD)	Min-Max	Mean (SD)	Min-Max	<i>p</i>
Avg. Pit Depth (h_p) (mm)	0.128 (0.019)	0.079-0.165	0.110 (0.022)	0.040-0.150	9.48E-05
Central Foveal Thickness (h_{cft}) (mm)	0.224 (0.016)	0.186-0.266	0.223 (0.014)	0.199-0.264	0.628
Avg. Rim Height (h_r) (mm)	0.352 (0.014)	0.319-0.389	0.335 (0.018)	0.285-0.378	5.75E-08
Avg. Rim Disk Diameter (d_r) (mm)	2.130 (0.190)	1.680-2.580	2.140 (0.170)	1.760-2.510	0.608
Rim Disk Area (A_r) (mm ²)	3.580 (0.660)	2.220-5.240	3.510 (0.590)	2.440-4.900	0.570
Major Axis Rim Disk (λ_r^1) (mm)	0.625 (0.110)	0.372-0.867	0.615 (0.100)	0.420-0.860	0.635
Minor Axis Rim Disk (λ_r^2) (mm)	0.535 (0.100)	0.320-0.817	0.524 (0.089)	0.330-0.780	0.576
Avg. Slope Disk Diameter (d_s) (mm)	0.608 (0.015)	0.340-0.955	0.636 (0.160)	0.274-1.010	0.358
Slope Disk Area (A_s) (mm ²)	0.313 (0.120)	0.100-0.710	0.348 (0.170)	0.059-0.839	0.270
Major Axis Slope Disk (λ_s^1) (mm)	0.053 (0.020)	0.019-0.123	0.060 (0.029)	0.010-0.839	0.080
Minor Axis Slope Disk (λ_s^2) (mm)	0.045(0.018)	1.00E-04-0.100	0.049(0.026)	2.00E-05-0.127	0.180
Avg. Pit Flat Disk Diameter (d_f) (mm)	0.182(0.031)	0.110-0.295	0.197(0.044)	0.100-0.433	0.083
Pit Flat Disk Area (A_f) (mm ²)	0.027(0.010)	0.011-0.068	0.033(0.018)	0.007-0.149	0.061
Major Axis Pit Flat Disk (λ_f^1) (mm ²)	0.004(0.001)	0.002-0.011	0.005(0.003)	0.001-0.025	0.053
Minor Axis Pit Flat Disk (λ_f^2) (mm ²)	0.004(0.001)	0.001-0.010	0.004(0.002)	0.001-0.022	0.069
Rim Volume (V_r) (mm ³)	1.020(0.190)	0.558-1.544	0.944(0.170)	0.597-1.364	0.023
Pit Volume (V_p) (mm ³)	0.239(0.044)	0.152-0.366	0.236(0.054)	0.134-0.384	0.766
Inner Rim Volume (V_{IR}) (mm ³)	0.110(0.018)	0.060-0.153	0.100(0.019)	0.062-0.147	0.019
Avg. Max. Pit Slope (s_m) (Degree)	12.740(2.680)	6.320-20.650	10.650(2.620)	3.400-16.290	1.38E-05
α_m (mm)	0.250(0.063)	0.133-0.470	0.250(0.077)	0.100-0.450	0.590
β_m (mm)	0.610(0.1)	0.360-0.830	0.560(0.089)	0.335-0.845	0.005

Funding

German Federal Ministry of Economic Affairs and Energy (BMW EXIST 03EFEBE079 to A.U.B., E.M.K. and T.O.), German Research Foundation (DFG Exc. 257 to F.P.) and German Federal Ministry of Education and Research (BMBF Neu² ADVISIMS to S. K. Yadav, S. Motamedi), and Berlin Institute of Health (BIH to F.C.O.)

Acknowledgments

The authors thank Janine Mikolajczak for technical support and Ulrich Reitebuch for his very helpful input regarding the mathematical model development.

Disclosures

S. K. Yadav, S. Motamedi, F. C. Oertel, E. M. Kadas, K. Polthier, T. Oberwahrenbrock have nothing to disclose. F. Paul serves on the scientific advisory board for the Novartis OCTIMS study; received speaker honoraria and travel funding from Bayer, Novartis, Biogen Idec, Teva, Sanofi-Aventis/Genzyme, Merck Serono, Alexion, Chugai, MedImmune, and Shire; is an academic editor for PLoS ONE; is an associate editor for Neurology Neuroimmunology and Neuroinflammation; consulted for Sanofi Genzyme, Biogen Idec, MedImmune, Shire, and Alexion; and received research support from Bayer, Novartis, Biogen Idec, Teva, Sanofi-Aventis/Genzyme, Alexion and Merck Serono. A.U. Brandt served on the scientific advisory board for the Biogen Vision study; received travel funding and/or speaker honoraria from Novartis Pharma, Biogen, Bayer and Teva; has consulted for Biogen, Nexus, Teva and Motognosis.